Experimental study of inertia-based passive deformation of a heaving and pitching airfoil operating in the energy harvesting regime

Firas F. Siala,[1] Kiana Kamrani Fard,[1] and James A. Liburdy[1, a)]

Experimental Fluid Mechanics Research Laboratory, Oregon State University, Corvallis, Oregon 97331, USA

(Dated: 15 July 2019)

The effects of passive, inertia-induced surface deformation at the leading and trailing edges of an oscillating airfoil energy harvester are investigated experimentally at reduced frequencies of $k = fc/U_\infty = 0.10$, 0.14 and 0.18. Wind tunnel experiments are conducted using phase-resolved, two-component particle image velocimetry to understand the underlying flow physics, as well as to obtain force and pitching moment estimates using the vortex-impulse theory. Results are obtained for leading and trailing edge deformation separately. It is shown that both forms of deformation may alter the leading edge vortex inception and detachment time scales, as well as the growth rate of the circulation. In addition, surface deformation may also trigger the generation of secondary vortical structures, and suppress the formation of trailing edge vortices. The total energy harvesting efficiency is decomposed into contributions of heaving and pitching motions. Relative to the rigid airfoil, the deforming leading and trailing edge segments are shown to increase the energy harvesting efficiency by approximately 17% and 25%, respectively. However, both the deforming leading and trailing edge airfoils operate most efficiently at $k = 0.18$, whereas the peak efficiency of the rigid airfoil occurs at $k = 0.14$. It is shown that the deforming leading and trailing edge airfoils enhance the heaving contribution to the total efficiency at $k = 0.18$ and the negative contribution of the pitching motion at high reduced frequencies can be alleviated by using a deforming trailing edge.

[a)]Electronic mail: liburdyj@oregonstate.edu

I. INTRODUCTION

The escalating demand for reducing dependence on fossil fuels has provided significant motivation toward the development of alternative and clean energy harvesting devices. One attractive energy resource is the wind, where typically rotational-based turbines are used to extract the kinetic energy of the flow. However, these traditional turbines possess several undesired economical as well as environmental impacts[1]. An alternative energy harvesting system that provides several advantages to more conventional rotating-based turbines is the oscillating airfoil energy harvester. These systems rely on the use of combined heaving and pitching airfoils to harvest energy at efficiencies ranging from 20% to 40%[2–5]. While these oscillatory-based devices have certainly been shown to be quite promising, there is potential for improved efficiency[6].

The concept of extracting flow energy using oscillating airfoils is inspired by the unsteady flapping flight of insects and birds[7–10]. The flapping/oscillating motion of these natural fliers induce large-scale unsteady flow separation that causes significant deviations from the well-known static aerodynamic lift curve, in a process known as dynamic stall. During dynamic stall, flow separates at the leading edge of the airfoil surface and subsequently rolls into leading edge vortices (LEVs). Polhamus[11] has shown that LEVs are beneficial to lift generation by producing a region of low pressure on the suction side of the airfoil, resulting in a strong suction force, as long as the LEV remains attached to the airfoil surface. Unlike rotary turbines where flow around the blades must be attached to the airfoil surface to achieve high efficiency, oscillating energy harvesters exploit the unsteady flow separation and LEV formation to attain high efficiency. Although the role of LEVs in forward flapping flight efficiency (i.e. thrust producing systems such as birds) is well documented[12,13], their effects on energy harvesting devices, which tend to operate in different flow regimes, are yet to be thoroughly explored.

The oscillatory/flapping motion of an airfoil operating in the energy harvesting regime is typically modeled as combined sinusoidal heaving and pitching motion. Then, the instantaneous power output of a heaving and pitching airfoil can be expressed as:

$$P = F_y \dot{h} + M_z \dot{\theta} \tag{1}$$

where F_y is the vertical force (i.e. perpendicular to the free stream flow), M_z is the aerodynamic moment about the pitching center of the airfoil, $\dot{h}$ is the heaving velocity and $\dot{\theta}$ is the pitching velocity. The vast majority of published studies on oscillating energy harvesters focused on optimizing the motion kinematics, mostly using numerical simulations[2,3,5,14,15] with fewer experimental

studies[16–18]. These results show that energy harvesting efficiency is maximized when the airfoil is oscillating at pitching amplitudes of 60°-80°, heaving amplitudes of 0.5c-1.0c (c is airfoil chord length) and reduced frequencies ($k = fc/U_\infty$, where f is oscillation frequency and U_∞ is the free stream velocity) of 0.12-0.16.

It can be seen from Eq. (1) that there are two main factors influencing the power output: (i) the magnitude of the force F_y and pitching moment M_z and (ii) the correlation between F_y and $\dot{h}$ as well as between M_z and $\dot{\theta}$. Several studies have been conducted in the past few years that investigate different mechanisms that enhance both the peak force and moment, as well as the correlation between the aerodynamic forces and airfoil motion[19–22]. One prominent mechanism is the use of structurally deforming airfoils. Previous studies on insect wings as well as micro-air-vehicles suggest that deformation near the trailing edge leads to the generation of higher thrust and lift forces[23–26]. Airfoil surface deformation can either be controlled or passive. In controlled surface flexibility, the deformation of the surface is prescribed and the effects of airfoil inertia and the fluid-structure interactions are neglected. Hoke *et al.*[27] used a two-dimensional (2D) laminar simulation with prescribed camber deformation to show that the energy harvesting efficiency is increased by 15.8% relative to a fully rigid airfoil. When the camber deformation is prescribed correctly, the timing of LEV formation and hence the correlation between the forces and airfoil motion is enhanced. Furthermore, Liu *et al.*[28] numerically modeled 2D oscillating airfoil energy harvesters with deforming leading and trailing edges. The motion of the deforming leading and trailing edges was predetermined based on *a priori* structural analysis. They show that airfoils with a deforming trailing edge enhance the strength of the LEV and resultant peak force magnitudes, whereas deformation at the leading edge controls the timing of LEV formation, and thus the correlation between the aerodynamic forces and airfoil motion. Interestingly, both leading and trailing edge controls shifted the peak efficiency to higher reduced frequencies compared to a rigid airfoil.

Passive surface deformation can be divided into two categories: (i) inertia-induced deformation and (ii) flow-induced deformation. Flow-induced deformation occurs when the airfoil density is comparable with the density of the surrounding fluid. Tian *et al.*[29] conducted a numerical model based on the immersed boundary method to compare the effects of passive deformation with controlled and rigid airfoils. Their results show that passive, flow-induced surface deformation at the leading edge improved the energy harvesting performance by only 1%, whereas controlled leading edge deformation increased the efficiency by 11.3% compared to a rigid airfoil. With controlled

deformation, the leading edge segment was set to deform such that it produced a smaller effective angle of attack compared to a rigid airfoil, which was shown to slow down the formation and detachment of the LEV. Consequently, the flapping airfoil takes advantage of the LEV presence for a longer period of time during the oscillation cycle. Conversely, passive deformation of the leading edge segment was shown to be very small, and as a result, it had minimal impact on the energy harvesting efficiency. Moreover, Liu *et al.*[30] studied the effects of passive trailing edge segment deformation on the performance. They determined that with appropriate structure-to-fluid density and natural frequency of the trailing edge segment, the efficiency is enhanced by 7.24%. The deforming trailing edge creates a camber that enhances the pressure difference between the upper and lower surfaces of the airfoil. The influence of inertia-induced deformation of the leading edge on the performance was investigated experimentally by Totpal *et al.*[17] at reduced frequencies of 0.04-0.08. While their results show that leading edge deformation reduces the energy harvesting efficiency by 10% relative to a rigid airfoil at $k = 0.08$, the negative effects of the deformation were shown to subside as k is increased from k = 0.04 to 0.08. It remains unknown whether at larger reduced frequencies, the effects of inertia-induced leading edge deformation become beneficial.

In this paper, we conduct wind-tunnel testing and particle image velocimetry (PIV) measurements to investigate the feasibility of using inertia-induced deformation at the leading and trailing edges of the airfoil in the range of k = 0.10 - 0.18. To the best of our knowledge, there exists no experimental data that validate the feasibility of using deforming airfoil surface in the range of reduced frequencies relevant to optimal energy harvesting performance. We are specifically interested in seeing whether the negative effects of inertia-induced deformation subside, and even become favorable at the optimal reduced frequency range. Due to the difficulty of directly measuring the aerodynamic forces in a highly unsteady airfoil motion in wind tunnels, we use the vortex-impulse theory[31] to estimate both the force and moment to calculate power output. We have previously used the vortex-impulse theory with success to estimate the aerodynamic forces and energy harvesting performance using velocity data obtained from PIV[18,32]. Our objective is to first understand the underlying flow physics associated with deforming surfaces, and then to quantify and compare the power output and energy harvesting efficiency of the deforming leading and trailing edge airfoils with a fully rigid one.

The rest of the paper is organized as follows. In section II, the experimental and data analysis techniques are described. In section III, we compare the effects of deforming the leading and trailing edges with a fully rigid airfoil on the vorticity field, LEV evolution and energy harvesting

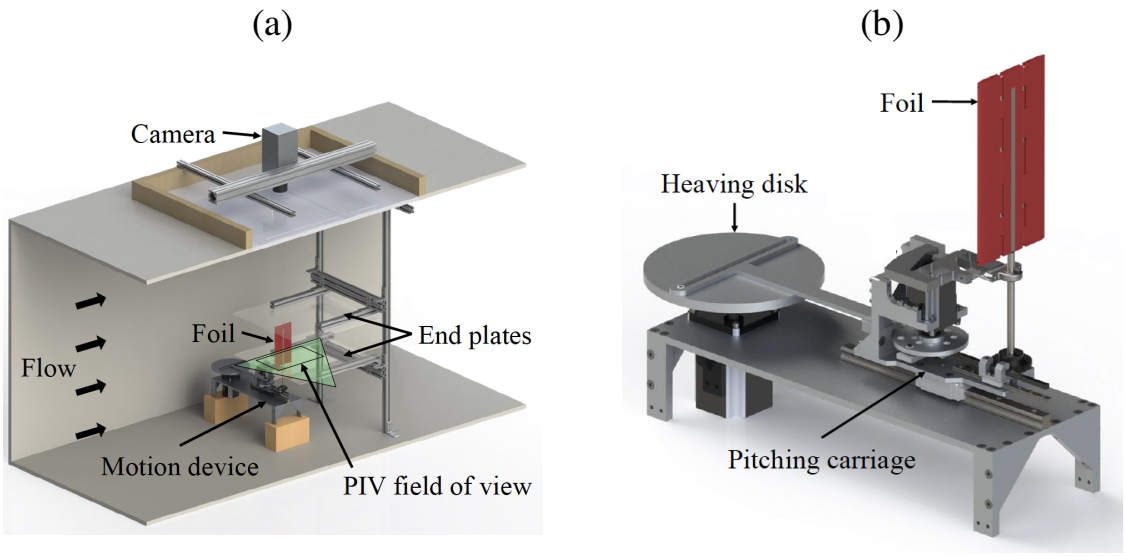

FIG. 1. (a) Drawing of the experimental setup illustrating the wind tunnel, motion device and PIV arrangement and (b) zoomed-in view of the motion device. Figures are adopted from[33] .

efficiency. In section IV, conclusions and implications of this work are provided.

II. METHODOLOGY

A. Experimental techniques

Fig. 1 shows the experimental setup in the wind tunnel and a zoomed-in view of the motion device used to achieve the airfoil motion. The wind tunnel is located at Oregon State University, and is a closed loop with a test section size of 1.37 m x 1.52 m with turbulence intensities below 2%. In addition, stationary end plates were placed approximately 2 mm from the airfoil tips to mimic quasi two-dimensional flow. The motion device consists of a scotch-yoke mechanism to generate the heaving motion and a combination of scotch-yoke and rack-and-pinion mechanisms to generate the pitching motion, according to the following:

$$h = h_0 cos(2\pi f t) \tag{2}$$

$$\theta = \theta_0 cos(2\pi f t + \Phi) \tag{3}$$

where h_0 is the heaving amplitude, θ_0 is the pitching amplitude and Φ is the phase-shift between heaving and pitching. The motion device was controlled using a LabVIEW program. The reduced

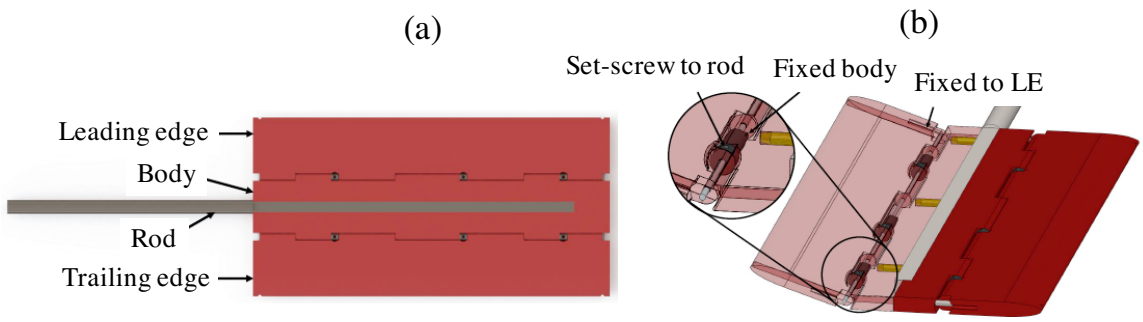

FIG. 2. (a) Top view of the airfoil and (b) detailed view of the airfoil LE/TE hinge mechanism.

frequency was varied by changing the free stream velocity while keeping the oscillation frequency fixed at 1.4 Hz. The Reynolds numbers ($Re = U_\infty c/\nu$, where ν is the kinematic viscosity) used in this study are 14189, 10135 and 7883 for k = 0.10, 0.14 and 0.18, respectively. The effect of Reynolds number at this low range has been found to have minimal impact on the energy harvesting performance[34].

The airfoil used in this study was manufactured in-house using fused deposition modeling and has a chord length, thickness and aspect ratio of 125 mm, 6.25 mm and 2, respectively. The airfoil leading and trailing tips are elliptical with 5:1 major to minor axis ratio. It consists of four acrylonitrile butadiene styrene (ABS) pieces and a machined titanium that is the three quarters the length of the airfoil span. The titanium rod provides structural support along the airfoil span to reduce span-wise flexibility. Two of the ABS pieces are attached to the titanium rod using pressed inserts to form the main body section of the airfoil. The remaining two ABS pieces consist of leading edge (LE) and trailing edge (TE) segments, each with a length of $c/3$. These segments are configurable to either rigidly attach to the airfoil main body, or serve as passively-actuated edges mimicking simplified surface deformation. The passive deformation of the LE or TE (LE/TE) was established by inserting a torsion rod into slots along both the main body and LE/TE, forming a hinge. The rod was secured at one end of the body and the other end to the LE/TE, providing a means to allow rotation of the LE/TE. A schematic of the airfoil and the hinge mechanism is shown in Fig. 2. Note that in this study, the flexible TE and LE configurations are investigated separately.

Two-component PIV measurements were obtained at the airfoil mid-span using a dual-head Nd:YAG pulsed laser (EverGreen, 145 mJ/pulse, max repetition rate of 15 Hz). A light sheet of approximately 1.5 *mm* thickness was generated at the mid-span of the airfoil using a LaVision

optics module. The wind tunnel was seeded with vegetable oil particles, which were generated using an in-house built Laskin Nozzle. Particle images were collected using a CCD camera (Image Pro, LaVision) with a resolution of 1600 $\times$ 1200 pixels. PIV images were processed with DaVis v8.4 software. The velocity fields were calculated using two passes of interrogation window size of 64 $\times$ 64 pixels, followed by two more passes of interrogation window size of 32 $\times$ 32 pixels, with an overlap of 50%. The time between the image pair was set such that an average of 8 pixel displacement per interrogation window was achieved in the streamwise direction. Velocity vectors were validated using a minimum correlation peak ratio of 1.2 as well as a moving-average validation scheme, where each velocity vector was replaced by the average of its neighbors if the difference between that velocity vector and its neighbors is greater than two standard deviations of the neighboring vectors. Overall, the percentage of velocity outliers was found to be approximately 2% of the entire velocity field. The velocity measurement uncertainty has been estimated using the correlation statistics technique[35]. The maximum uncertainty of the streamwise and cross-stream velocity components were found to be 3.5% and 5.8% of their respective maximum values. The velocity errors are then propagated to determine the uncertainty in vorticity and aerodynamic loadings. Detailed analysis of the propagation method can be found in[36]

A total of 126 phases during the downstroke motion with a sampling time of $\Delta t/T = 0.004$ were acquired. For each phase, one hundred images were acquired to calculate the phase-averaged velocity fields. The PIV system and airfoil motion were synchronized using LabVIEW. In order to obtain velocity data in the shadow region caused by the presence of the airfoil, the experiments were repeated at a phase delay of 180° for each phase of interest. The 180° out of phase flow fields were then mirrored and stitched to the rest of the vector field to construct the full flow field surrounding the airfoil. This can be done because the flow, airfoil shape and motion are all symmetric. Additionally, a second camera was used to capture the flow field in the downstream region. The two cameras were overlapped by 14 vectors and the overlapped region was smoothed with a 3$\times$3 moving-average filter.

B. Vortex-impulse theory: force and moment estimation

As previously mentioned, direct force and moment measurements of highly unsteady airfoils operating with large amplitudes of motion in wind tunnels are often not feasible. The difficulty is due to the airfoil inertial forces being in the same order of magnitude as the aerodynamic forces

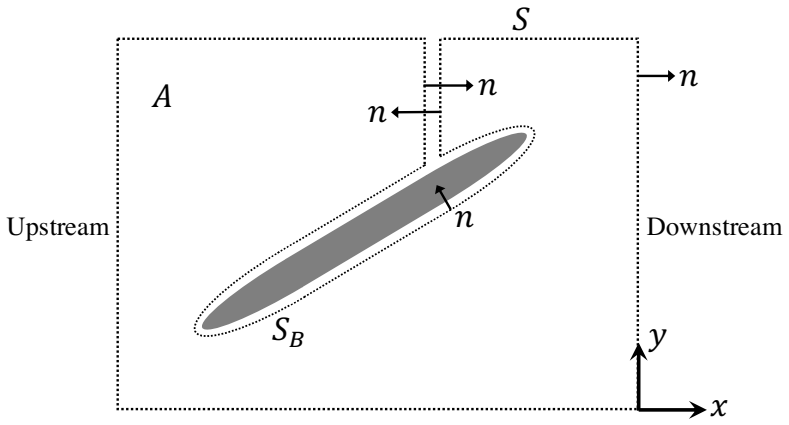

FIG. 3. Control volume used for impulse-based force and moment calculation.

or larger for reduced frequencies relevant to energy harvesting applications[33]. Since flow over oscillating airfoils operating in high amplitudes of motion is dominated by large scale vortical structures, it is then ideal to describe the aerodynamic loadings based on the dynamics of these vortical structures. In fact, the vorticity/circulation of these vortical structures indirectly represent the momentum imparted by the moving airfoil to the fluid. Wu[37] and Lighthill[38] have independently shown that forces generated by an airfoil can be obtained by taking the time-derivative of the vortex impulse, $\mathbf{P_F}$, which, in two-dimensional flows, is defined as:

$$\mathbf{P_F} = \int \mathbf{x} \times \boldsymbol{\omega} dA \tag{4}$$

where $\mathbf{x}$ is the position vector and A is the area occupied by the fluid. Lighthill explains that this expression is related to the total impulse (in the classical mechanics sense) required to establish a vorticity field, $\boldsymbol{\omega}$, from rest. For two-dimensional flows, Siala and Liburdy[32] have shown that the total force acting on the airfoil in a finite control volume can be written as:

$$\mathbf{F} = -\rho \frac{d\mathbf{P_F}}{dt} + \rho \oint_S \mathbf{n} \cdot \left(\frac{1}{2} [\mathbf{u} \cdot \mathbf{u}] \underline{\mathbf{I}} - \mathbf{uu} \right) dS \tag{5}$$

where $\underline{\mathbf{I}}$ is the identity tensor, $\mathbf{n}$ is the normal vector pointing away from the fluid and S is the external surface of the control volume. The second term of Eq. (5) represents the effects of vorticity shed in the far wake on the forces. For suddenly-accelerated bodies from rest where all the vorticity is captured in the control volume, this term can be shown to equal zero[39]. The finite-domain impulse equation originally derived by Noca[40] contains other additional terms. However, Siala and Liburdy[32] have shown that by selecting an origin location of the position vector located anywhere

along y-axis of the downstream control volume boundary (see Fig. 3), these additional terms that are included in Noca's equation become negligible, thus significantly simplifying the force equation to the expression given in Eq. (5). This can be done because the force equation is theoretically independent of the origin location. Experimentally, however, it is well known that errors in force calculation can be significantly amplified by the origin location[40]. We have determined in our previous study that the error associated with the origin location can be significantly reduced by setting the origin location at the downstream boundary, located at least one chord length from the trailing edge[32]. For a thorough discussion on practical considerations of the impulse-based force method, refer to the studies conducted by DeVoria *et al.*[41] and Siala and Liburdy[32]. Moreover, because the experiments are conducted in air, the added-mass of the airfoil is determined to be very small and therefore neglected in Eq. (5). Validation of the force estimation based on the impulse method is provided in[32].

Similarly, the vortex impulse associated with the aerodynamic moment, $\mathbf{P_M}$, can be defined as:

$$\mathbf{P_M} = \frac{1}{2}\int (\mathbf{x}\cdot\mathbf{x})\boldsymbol{\omega} dA \tag{6}$$

The aerodynamic moment can then be shown to be written as[18,31]:

$$\mathbf{M} = \rho\frac{d\mathbf{P_M}}{dt} - \rho\int \mathbf{x}\times(\mathbf{u}\times\boldsymbol{\omega})dA - \rho\frac{1}{2}\oint(\mathbf{x}\cdot\mathbf{x})\mathbf{n}\times(\mathbf{u}\times\boldsymbol{\omega})dS \tag{7}$$

Since we are interested in the moment about the pitching center of the airfoil, we fixed the origin location at the pitching axis of the airfoil, which is located at the mid-chord. The maximum uncertainty of the instantaneous force and moment were found to be 10.6% and 13.2% of the peak force and moment, respectively.

C. Pressure calculation from PIV data

In many cases, the mechanisms of force and moment production can be illuminated by visualizing the pressure field. To do this, we use the algorithm described by Dabiri *et al.*[42] to calculate the pressure field from phase-averaged velocity data. Briefly, the algorithm is used to perform a direct integration of the pressure gradient term in the Navier-Stokes equations along eight paths through each point in the flow field. The starting point of all eight integration paths is located at the control volume boundary. The median of the pressure value obtained from all eight integration paths is then used to estimate the pressure at each point in the field. Although the pressure fields

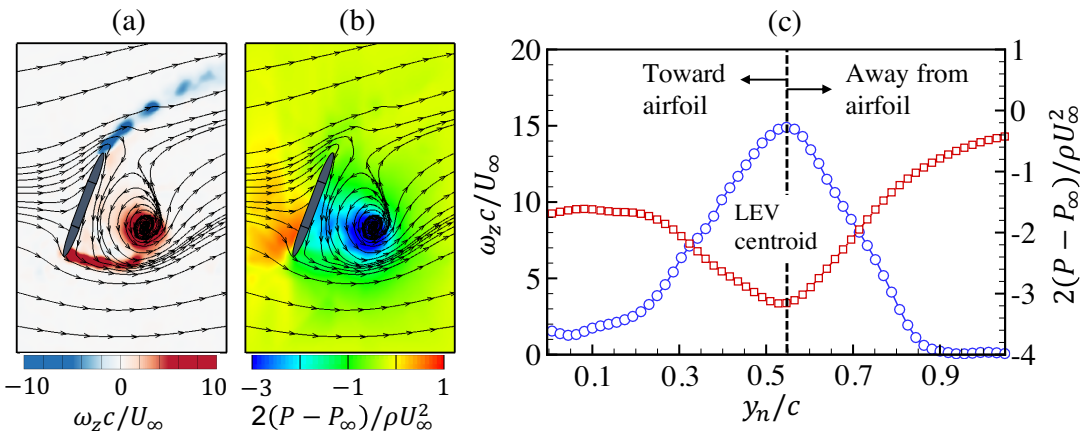

FIG. 4. (a) Vorticity field and streamlines and (b) pressure field and streamlines for k = 0.10 at the mid-downstroke. (c) Wall-normal profile of the vorticity and pressure through the LEV center. The blue circles represent the vorticity and the red squares represent the pressure.

obtained using this method are not sufficiently accurate for force evaluation in our current experimental setup, we present the pressure fields for qualitative purposes, to provide more insight in interpretation of the results. The pressure field is qualitatively validated in Fig. 4. In Fig. 4(a) and 4(b), the non-dimensional vorticity and pressure fields, along with the flow streamlines, are shown for $k = 0.10$ for the rigid airfoil case. It is shown that the pressure and vorticity fields are well correlated, with the pressure minima and maxima being generated in the LEV core and on the upper surface of the airfoil (stagnation point), respectively. The wall-normal profiles of the vorticity and pressure are shown in Fig. 4(c). The wall-normal distance, y_n/c, is equal to zero at the airfoil surface. The profile is drawn through the LEV center, which is detected by the maximum vorticity value. As expected, the peak vorticity and pressure are shown to correlate very well. Going away from the surface, the pressure slowly approaches free stream pressure and the vorticity decays rapidly to $\omega_z c/U_\infty = 0$

III. RESULTS

In this section, we present results for rigid, flexible LE and flexible TE airfoils operating at reduced frequencies, k, of 0.10, 0.14 and 0.18, while holding the heaving amplitude, pitching amplitude, phase shift and pitching axis fixed at $h_0/c = 0.6$, $\theta_0 = 75°$, $\Phi = 90°$ and $x_p/c = 0$

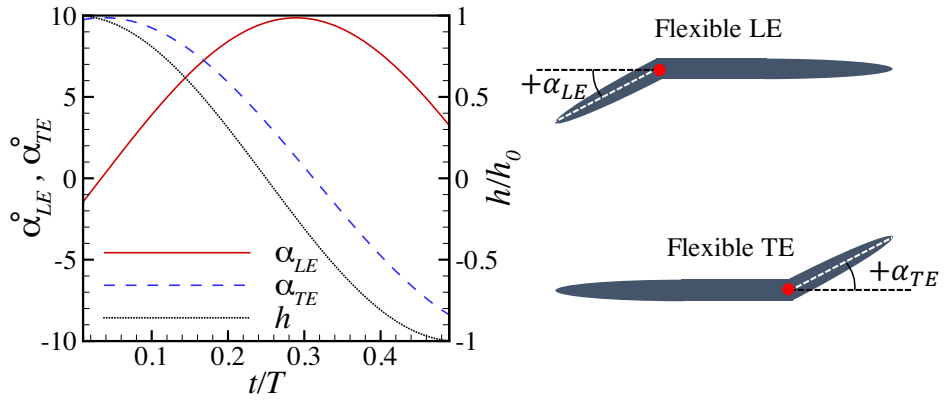

FIG. 5. Leading and trailing edge deformation angle relative to the airfoil chord as a function of time during the downstroke motion. The heaving motion, h, is also shown for reference. Positive angles indicate that the LE/TE are deformed counter-clockwise relative to the airfoil main body.

(mid-chord). Due to the symmetry of the problem, the results are only provided for the downstroke motion of the airfoil.

A. Leading and trailing edge deformation motion

Before analyzing their effects on the flow physics, it is important to report the motion of the passive deformation of the leading and trailing edges during the oscillation cycle. Key parameters that determine the degree of deformation are the torsion spring natural frequency and the linear density of the LE/TE. The natural frequency can be defined as $f_N = 1/2\pi\sqrt{\tau/I_m}$, where τ is the spring constant and I_m is the moment of inertia about the hinge. The torsion spring constant was calculated by attaching a known mass to the LE/TE while the wing was static. Images of the downward deflection were recorded and used to calculate the angle of deflection, $\theta_{LE/TE}$. The torsion spring constant is calculated using $\tau = \frac{T}{\theta_{LE/TE}}$, where T is the torque applied to the LE/TE. Following Liu *et al.*[30], the natural frequency of the deforming LE/TE is non-dimensionalized as $f_N^* = f_N c/U_\infty$, to obtain f_N^* of 0.6, 0.85 and 1.1 for k of 0.10, 0.14 and 0.18, respectively. Furthermore, the linear density of the LE/TE segments, $\rho_l = s\rho_{LE/TE}$ (where s is airfoil thickness and $\rho_{LE/TE}$ is the density of the LE/TE) is normalized by the fluid density ρ and airfoil chord length c to obtain the structure-to-fluid density ratio $\mu = \rho_l/c\rho$. The structure-to-fluid density used in this study is $\mu = 27.3$, which is significantly higher than the values of μ = 0.03-0.6 used

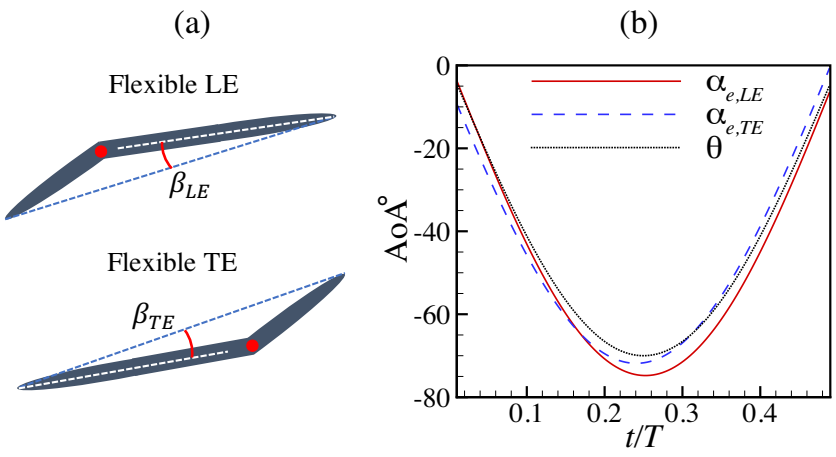

FIG. 6. (a) Schematic sketch showing the angle β induced by the leading/trailing edge motion and (b) effective angle of attack induced by the leading and trailing edge deformation. For reference, the pitching angle, θ, is also shown.

by Liu *et al.*[30]. A large value of the structure-to-fluid density is used in this study to reduce the effects of the flow on deformation and enhance the magnitude of the inertia-based deformation of the LE/TE.

In Fig. 5, the deformation angle of the leading and trailing edges are shown in degrees as a function of time during the downstroke motion of the airfoil. Positive angles indicate that the LE/TE are deflected counter-clockwise relative to the airfoil main body. It can be seen that there is an approximately 90° phase-lag between the motion of the LE and TE. The peak positive angle of deformation of the LE occurs approximately during the mid-downstroke, whereas the positive peak deformation angle of the TE occurs as the airfoil undergoes motion reversal at the beginning of the downstroke. Measurement of the deformation angle was conducted with and without free stream flow, and the results were found to be essentially identical. Since we are varying the reduced frequency by changing only the free stream velocity while keeping the oscillation frequency fixed, the deformation angles are the same for k = 0.10-0.18. Furthermore, the geometric effective angle of attack induced by the deformation of the leading and trailing edges can be defined as follows:

$$\alpha_{e,LE/TE} = \theta + \beta_{LE/TE} \tag{8}$$

where $\beta_{LE/TE}$ is the interior angle measured from the lines from the leading edge to the trailing edge tips and along the chord of the main airfoil body, as shown in Fig. 6(a). In Fig. 6(b), the angle of attack (AoA) induced by the leading and trailing edges, as well as the pitching angle are shown

during the downstroke. As can be clearly seen, the deformation of the leading edge enhances the AoA compared to a rigid airfoil (whose geometric AoA is simply equal to θ), throughout most of the downstroke. On the other hand, the deforming trailing edge case is shown to enhance the the AoA up until $t/T \approx 0.3$. For $t/T > 0.3$, the motion of the trailing edge segment is reversed, resulting in a smaller AoA compared to the rigid airfoil.

B. Vorticity field characterization

The vorticity field was calculated from velocity using a central difference scheme. The average uncertainty was found to be approximately 4.7% of the maximum vorticity[36]. Snapshots of the vorticity field evolution for the rigid, flexible LE and flexible TE airfoils operating at $k = 0.10$ are shown in Fig. 7. As the airfoil begins its downstroke motion, the flow on the upper surface of the airfoil is still not fully attached due to the flow separation that occurred during the upstroke motion. As time progresses, the flow eventually begins to attach on the upper surface and separates at the leading edge of the bottom surface to form a counter-clockwise rotating LEV. At $t/T = 0.15$, it can be seen that the LEV generated by the flexible LE and TE airfoils is slightly larger than the LEV of the rigid airfoil. At $t/T = 0.25$, the LEV is shown to be lifted-off from the lower airfoil surface for all three cases, while the trailing edge vorticity continues to shed into the wake. The trailing edge vortex sheet sheds in a similar manner for the rigid and flexible LE cases, whereas for the flexible TE case the vorticity is shown to have a more pronounced curved trajectory. Furthermore, the LEV size keeps increasing as long as the leading edge shear layer keeps feeding the LEV with vorticity. Eventually, the shear layer strength begins to decay and it disconnects from the LEV. At $t/T = 0.35$, the shear layer of the flexible TE airfoil begins to roll into discrete small-scale vortex structures in the from of a Kelvin-Helmholtz-like instability, whereas for the rigid and flexible LE cases the shear layer vorticity appears to be confined in a more continuous vortex sheet. As the airfoil approaches the end of the downstroke at $t/T = 0.45$, the shear layer is shown to be completely disconnected from the LEV for both the rigid and flexible TE cases, whereas it appears to remain loosely connected to the LEV in the flexible LE case. Moreover, as the LEV convects downstream past the airfoil trailing edge, it causes the trailing edge shear layer to form into a large distinct trailing edge vortex (TEV). Several studies have described this process as a bluff-body like vortex shedding, where the flow from the upper surface of the airfoil and LEV forms a saddle point near the trailing edge, which forces the trailing shear layer to roll into a TEV[43–45]. On the other

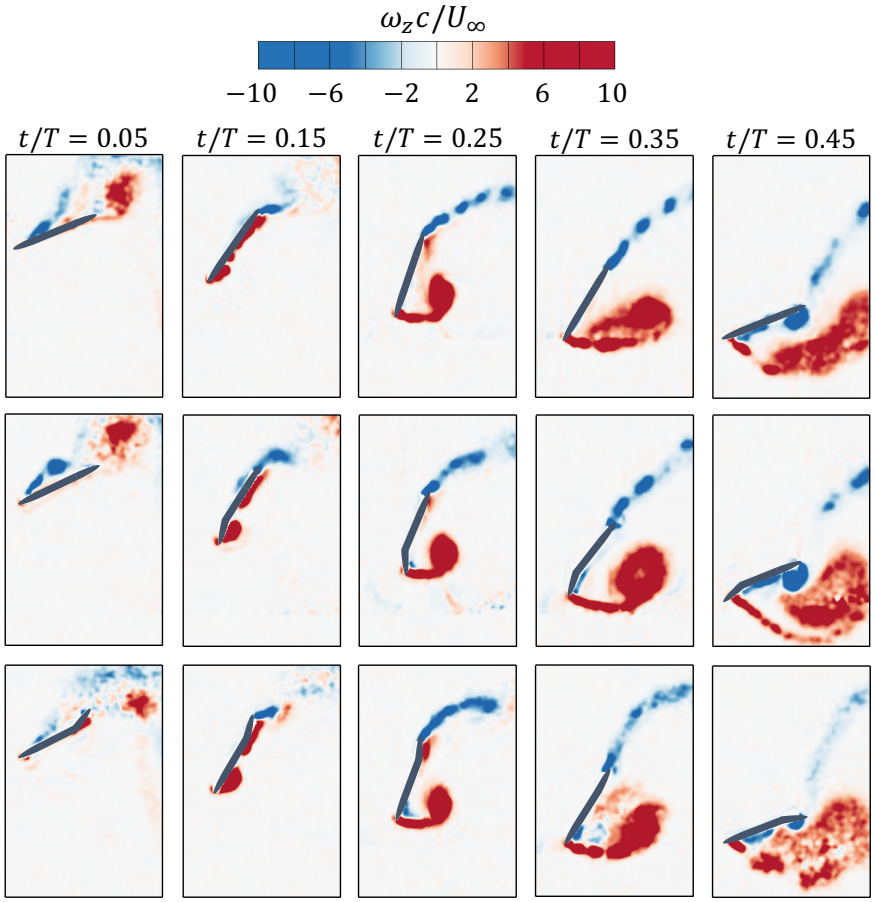

FIG. 7. Non-dimensional vorticity field at $k = 0.10$ for the rigid (top row), flexible LE (middle row) and flexible TE (bottom row) airfoils during the downstroke motion.

hand, the TEV formation is significantly suppressed by the flexible TE airfoil. At $t/T \approx 0.35$, the trailing edge segment begins to deform clockwise relative to the airfoil main body (see Fig. 5) and it becomes almost parallel with the streamwise flow at $t/T = 0.45$. As a result, the flow leaving the trailing edge from the upper surface tends to be more aligned with the streamwise flow, thus significantly reducing the velocity gradient near the airfoil trailing edge.

In Fig. 8, the vorticity evolution for $k = 0.14$ for all three cases is shown. The evolution process of the LEV remains the same as for $k = 0.10$, with few noticeable differences as described here. Firstly, as the airfoil downstroke begins, significant negative vorticity remains in close proximity to the airfoil. This is associated with the LEV generated from the upstroke motion. With increasing reduced frequency, the flow convection time scale increases relative to the time scale of airfoil motion, and therefore the airfoil captures the LEV during motion reversal before the LEV completely

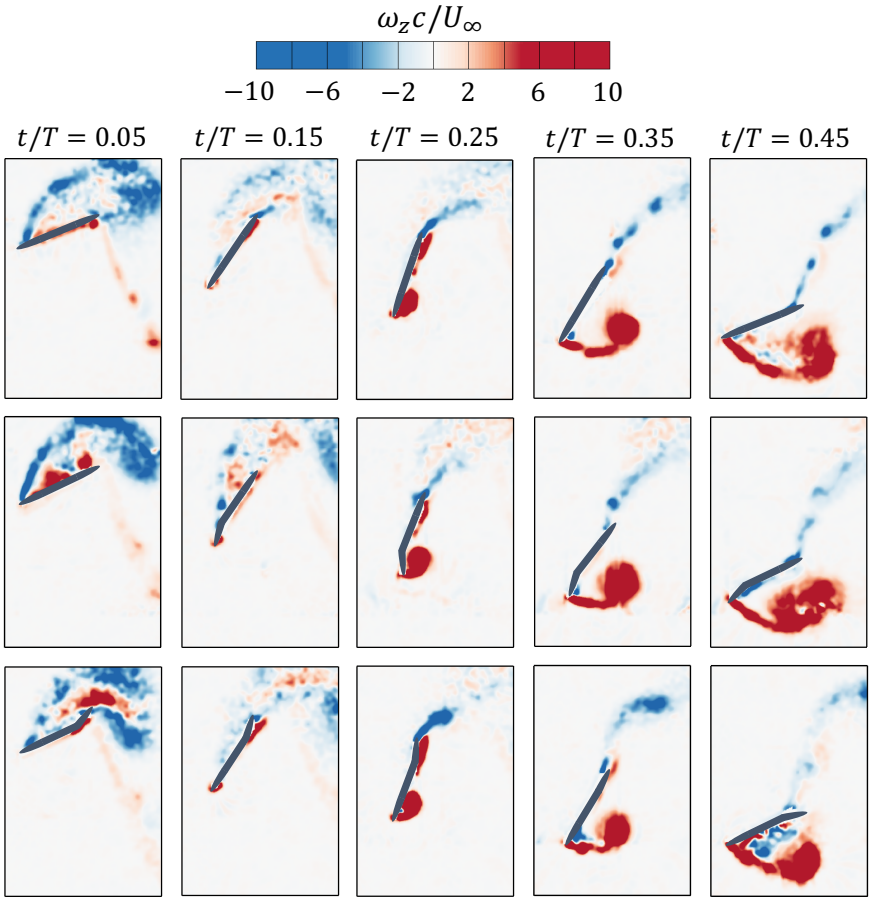

FIG. 8. Non-dimensional vorticity and velocity fields at $k = 0.14$ for rigid (top row), flexible LE (middle row) and flexible TE (bottom row) airfoils during the downstroke motion. Note that only every other velocity vector is shown.

convects into the wake. Secondly, the inception time of the LEV is delayed to later in the cycle at higher reduced frequencies. Furthermore, at $t/T = 0.25$, the LEV is shown to remain attached to the airfoil surface, compared with the earlier detachment for $k = 0.10$. The LEV generated by the flexible LE case is also shown to be slightly larger than the LEV of the rigid and flexible TE case. Compared to $k = 0.10$, the LEV of the flexible TE case grows at a slightly slower rate due to the decrease in the deformation angle of the TE at this instant, as shown in Fig. 6(b). As time progresses, the LEV size remains fairly constant for the rigid and flexible TE cases at $t/T > 0.35$, whereas it keeps growing until $t/T = 0.45$ for the flexible LE case. As the airfoil approaches the end of the downstroke, the LEV begins to convect past the airfoil trailing edge, however no TEV formation is observed. This is because by the time the LEV approaches the airfoil trailing edge,

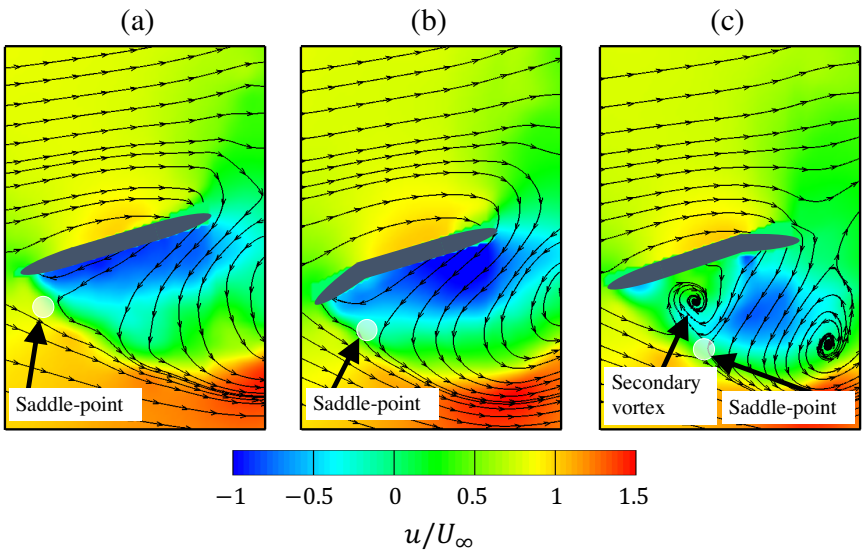

FIG. 9. Zoomed-in view of the streamwise velocity contours and streamlines at $k = 0.14$ and $t/T = 0.45$ for (a) rigid, (b) flexible LE and (c) flexible TE airfoils.

the angle of attack of the airfoil is quite small, such that the trailing edge shear layer is not strong enough to roll into a distinct TEV structure. At $k = 0.14$, the vortex shedding in the wake switches from 2P to 2S, where the former represents two pairs of vortical structures (LEV and TEV) shed per oscillation cycle, and the latter represents two single vortices shed per oscillation cycle (one LEV per half cycle)[46]. Lastly at $t/T = 0.45$, it can be seen in the flexible TE case that there is a clockwise rotating vortex entrapped between the airfoil and the LEV. Because the TE segment is almost aligned with the streamwise flow, the flow from the upper surface of the airfoil loses a significant amount of its streamwise momentum as it turns around the trailing edge. In fact, much of the flow reversal around the trailing edge for the flexible TE case is caused by flow entrainment of the LEV. The evidence for this is supported by Fig. 9 where the streamwise velocity contours are shown for the three different cases at $t/T = 0.45$. As the relatively slow moving flow reversal travels upstream toward the airfoil leading edge, it eventually interacts with the separated leading edge shear layer to form a saddle-point. At the saddle point, the flow traveling upstream from the trailing edge bifurcates and it either gets entrained by the shear layer or it travels upstream and upward toward the airfoil surface. Since flow reversal of the flexible TE case has relatively small streamwise momentum and therefore cannot travel upstream for long, it eventually begins to roll to form a clockwise rotating secondary vortex.

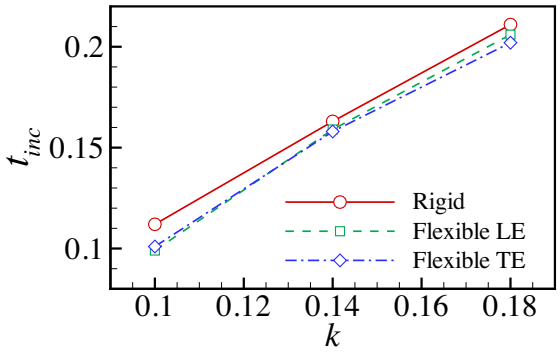

FIG. 10. Estimate of the LEV inception time (normalized by oscillation period) versus reduced frequency for the rigid, flexible LE and flexible TE airfoils.

C. Inception of the leading edge vortex

We have briefly mentioned above that increasing the reduced frequency delays the inception/formation of the LEV. The mechanism leading to LEV inception occurs at the boundary-layer scale, which we cannot resolve using the current experimental set-up. However we can approximate the time scale of the inception visually, by noting the time at which a small vorticity bubble begins to form on the airfoil. Fig. 10 shows the approximated LEV inception time scale, t_{inc} (normalized by the oscillation period), versus reduced frequency for the rigid, flexible LE and flexible TE airfoils. As can be clearly seen, the inception time seems to be approximately linearly increasing with k, where the deforming leading and trailing edge airfoils slightly reduce the inception time of the LEV. This delay in LEV inception is actually a result of the decrease in vorticity flux at the airfoil surface with increasing k. The vorticity flux from the airfoil surface is proportional to the shear layer velocity near the airfoil leading edge, U_{SL}[47]. The rate of vorticity/circulation growth of the LEV can be approximated as[48]:

$$\frac{d\Gamma_{LEV}}{dt} = -\frac{1}{2}U_{SL}^2 \tag{9}$$

where Γ_{LEV} is the LEV circulation. We can approximate the shear layer velocity as the vector sum of the local velocity of the leading edge and the component of the free stream velocity in the direction of airfoil motion:

$$U_{SL} \approx U_\infty sin(\theta) - \dot{h}cos(\theta) - \frac{\dot{\theta}c}{2} \tag{10}$$

In Fig. 11(a), the flow velocity at the leading edge normalized by the maximum airfoil tip velocity is shown for $k = 0.10$, 0.14 and 0.18. As can be clearly seen, the shear layer velocity decreases with

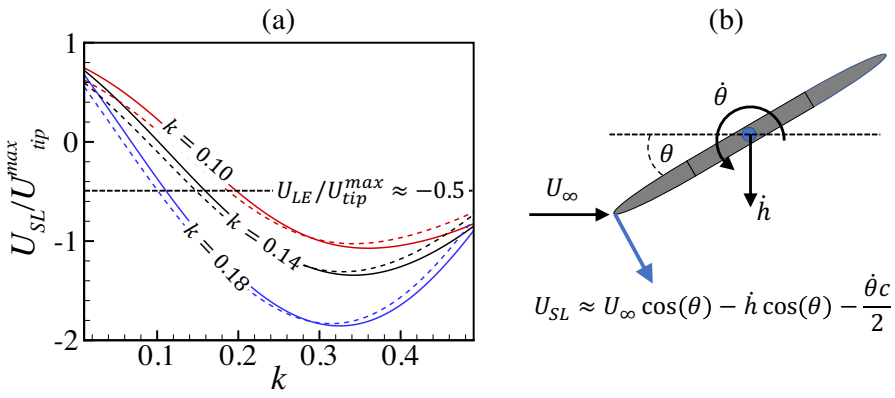

FIG. 11. (a) Normalized shear layer velocity at the leading edge for k = 0.10-0.18. The solid lines represent the velocity of the rigid airfoil and the dashed lines represent velocity of the flexible LE airfoil. (b) Sketch of the velocity vectors used to approximate U_{SL}

increasing k. Consequently, the smaller vorticity flux at higher k values delays the LEV inception time. It is also interesting to point out that the LEV inception time scale shown in Fig. 10 coincides with the time at which the non-dimensional leading edge velocity is approximately equal to 0.5 for all the reduced frequencies that we test. Furthermore, we can also approximate the leading edge tip velocity for the flexible LE airfoil, $U_{SL_{Flexible}}$, as follows:

$$U_{SL_{Flexible}} \approx U_\infty sin(\theta) - \dot{h}cos(\theta) - \frac{\dot{\theta}c}{2} - \frac{c\dot{\alpha}_{LE}}{3} \tag{11}$$

where the additional term, $c\dot{\alpha}_{LE}/3$, represents the leading edge tip velocity. The approximate shear layer velocity of the flexible LE airfoil is also shown in Fig. 11(a) (dashed lines). We can see that the motion of the deforming leading edge segment slightly increases the shear layer velocity during the first half of the down-stroke. Interestingly, the timing of the non-dimensional velocity $U_{SL}/U_{tip}^{max} \approx -0.5$ also coincides with the timing of the LEV inception for the flexible LE. Note that while the flexible TE has a rigid leading edge, its LEV inception time is also shown to decrease relative to the rigid airfoil. We believe that this is associated with the enhanced effective camber provided by the deformed trailing edge, which could accelerate the flow at the leading edge to yield a larger U_{SL} than the rigid airfoil.

The implication of this discussion is that the non-dimensional shear layer velocity can be used to approximate the inception time of the LEV, which may be of great importance in developing potential flow-based models of oscillating airfoils undergoing dynamic stall[49].

D. Effects of surface deformation on leading edge vortex evolution

It is well known that the circulation generated by airfoils is a manifestation of the momentum imparted to the flow field and therefore is directly related to the production of aerodynamic forces. Here, we analyze the role of deforming LE and TE on the time-history of LEV circulation. To determine the boundaries of LEVs, we use the γ_2 method proposed by Graftieaux *et al.*[50], which is given by:

$$\gamma_2(P) = \frac{1}{S_A}\int_{M\in S_A} \frac{[\mathbf{PM}\times(\mathbf{U_M}-\overline{\mathbf{U}}_\mathbf{P})]\cdot n_z}{||\mathbf{PM}||\cdot||\mathbf{U_M}-\overline{\mathbf{U}}_\mathbf{P}||} dS_A \tag{12}$$

where S_A is the area of integration, $\mathbf{P}$ is any point in the flow field, $\mathbf{M}$ is any point within the integration area, $\overline{\mathbf{U}}_\mathbf{P}$ is the average velocity within the integration area, $\overline{\mathbf{U}}_\mathbf{M}$ is the velocity of point M in the integration area, $\mathbf{PM}$ is the distance between $\mathbf{P}$ and $\mathbf{M}$ and n_z is the normal vector in the z direction. The vortex boundary is given by $|\gamma_2| = 2/\pi$. The LEV circulation, Γ_{LEV}, can then be computed by integrating the vorticity enclosed by the contour level of $|\gamma_2| = 2/\pi$:

$$\Gamma_{LEV} = \int_{|\gamma_2|=2/\pi} \omega_z dA \tag{13}$$

where ω_z is the spanwise vorticity. As stated previously, it is not possible to determine the LEV strength as soon as it initiates due to the inability to resolve the boundary-layer scale with the current experimental setup, and therefore we only report the circulation once sufficient development occurs for the γ_2 method to capture the LEV. LEVs are then tracked until they begin to convect downstream outside of the control volume. The LEV circulation, non-dimensionalized by the free stream velocity and airfoil chord length, is shown in Fig. 12 for k = 0.10, 0.14 and 0.18. As the LEV forms, it grows in strength as it entrains vorticity from the leading edge shear layer. Therefore, the shear layer strength is a crucial parameter in determining the LEV circulation, as well as the rate of circulation growth. It is shown for $k = 0.10$ that the LEV of the flexible LE airfoil grows, on average, at a faster rate than the LEV of the rigid and flexible TE airfoils. This is attributed to the stronger shear layer generated by the larger camber created by the deforming LE segment. Furthermore, the LEV keeps increasing in strength until it is detached from the feeding shear layer. Different mechanisms of LEV detachment in flapping airfoils have been proposed by Widmann and Tropea[44]. In one of the mechanisms, which they refer to as bluff-body-like vortex detachment, the flow reversal from TEVs that travels upstream towards the leading edge interacts with the feeding shear layer to decrease its velocity, such that it no longer keeps up with the downstream convecting LEV. At $k = 0.10$, where TEVs do form, the LEV for both the rigid and flexible

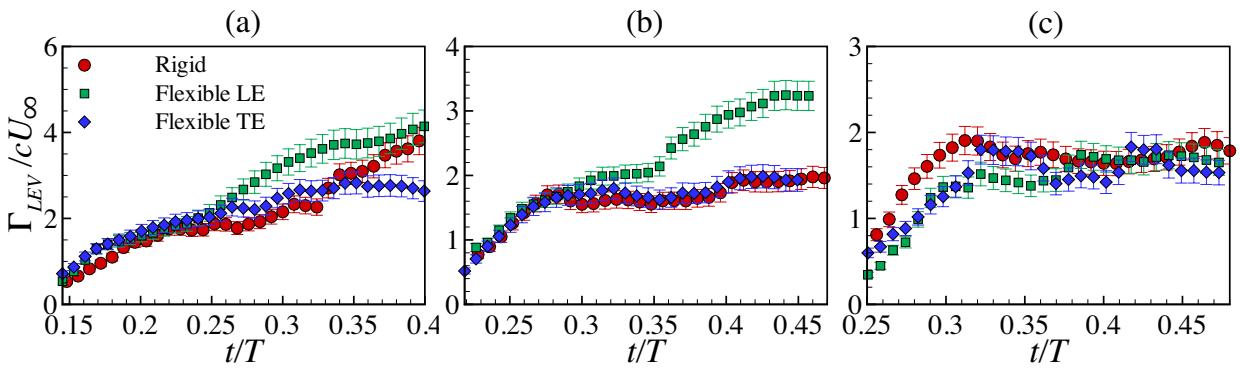

FIG. 12. Time-history of the non-dimensional LEV circulation for rigid, flexible LE and flexible TE airfoils at (a) $k = 0.10$, (b) $k = 0.14$ and (c) $k = 0.18$. For clarity, only every other data point is shown.

LE keeps increasing in strength until it reaches a maximum value of approximately $\Gamma_{LEV}/cU_\infty \approx 4$ at $t/T \approx 0.40$. This time approximately coincides with the formation time of the TEV, which indicates that bluff-body-like vortex detachment is the mechanism responsible of LEV detachment from its shear layer for the rigid and flexible LE airfoils. On the other hand, the flexible TE airfoil is shown to peak at $t/T \approx 0.35$, at a much lower circulation value of $\Gamma_{LEV}/cU_\infty \approx 3$. Because the flexible TE case suppresses the formation of the TEV, there must be another mechanism that is responsible for cutting-off the vorticity supply to the LEV. We suspect that the LEV is detached as a result of the interaction of the boundary layer with the feeding shear layer, in a process known as the boundary layer eruption[44,51]. In this process, the interaction of the LEV with the airfoil surface induces an adverse pressure gradient in a local region inside the boundary layer. As a result, the fluid elements in this region are compressed in the streamwise direction and consequently, a thin fluid layer is squeezed up from the interior of the boundary layer that erupts the shear layer, eventually cutting off the vorticity supply to the LEV. With the current experimental setup, we are unable to resolve this mechanism since it occurs at the boundary layer scale. However, regardless of the exact mechanism of LEV detachment, one can anticipate the onset of LEV detachment by closely examining the behavior of the feeding shear layer. Shortly prior to detachment, a Kelvin-Helmholtz-like (KH) instability in the shear layer is observed, where the shear layer begins to roll into discrete vortical structures and eventually gets disconnected from the LEV. This process is demonstrated in Fig. 13.

By increasing the reduced frequency to $k = 0.14$ (shown in Fig. 12(b)), the LEV circulation for the flexible TE and rigid airfoils follow the same trend, where they both peak at $\Gamma_{LEV}/cU_\infty \approx 2$

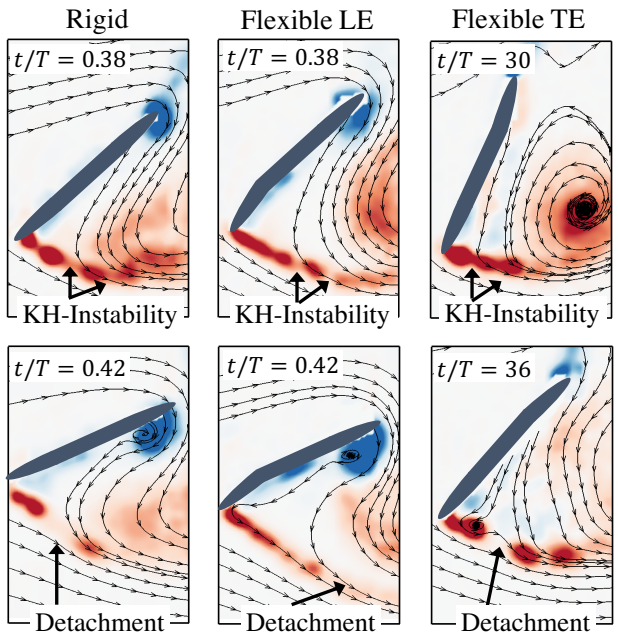

FIG. 13. Detachment process of the LEV from its feeding shear layer at $k = 0.10$. (Top) Zoomed-in view of vorticity field shortly prior to LEV detachment and (bottom) zoomed-in view of vorticity field after LEV detachment.

at $t/T \approx 0.30$. On the other hand, the flexible LE airfoil is shown to increase the LEV circulation until $t/T \approx 0.45$, with a maximum circulation of $\Gamma_{LEV}/cU_\infty \approx 3$. We believe that this is again related to the enhanced shear layer strength of the flexible LE airfoil. Future studies that include high-resolution investigation of the shear layer velocity will be conducted to better understand the shear-layer enhancement process. Finally in Fig. 12(c), the LEV circulation is shown for $k = 0.18$. For all three cases, the time-history of LEV circulation is shown to follow a similar trend to $k = 0.14$ (except for the flexible LE case), where surface deformation has no effect on the circulation. For all cases, the LEV reaches a peak value of approximately $\Gamma_{LEV}/cU_\infty \approx 2$ at $t/T \approx 0.325$. For completeness, the time scale of LEV detachment from its feeding shear layer is plotted in Fig. 14 as a function of the reduced frequency. The detachment time scale, t_{det}, is defined as the time at which the LEV circulation becomes constant.

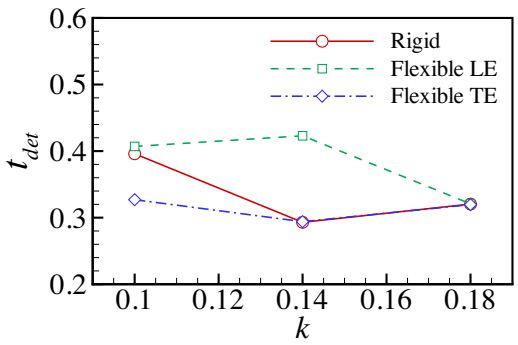

FIG. 14. Estimate of the LEV detachment time (normalized by oscillation period) versus reduced frequency for the rigid, flexible LE and flexible TE airfoils.

E. Impulse-based force and moment evaluation

The vertical component of force coefficient ($C_y = 2F_y/\rho U_\infty^2 c$) and spanwise moment coefficient ($C_m = 2M_z/\rho U_\infty^2 c^2$) are shown in Fig. 15 for $k = 0.10$ and 0.14. The heaving and pitching velocities of the airfoil are also shown. For $k = 0.10$, the flexible LE and TE airfoils are shown to increase the peak force by 14.7% and 12.7% relative to the rigid airfoil, respectively. The peak moment coefficient occurs slightly after the peak forces are produced. After its formation, the LEV remains near the upstream portion of the airfoil, which results in generating a negative, counter-clockwise pitching moment. The peak moment coefficient does not seem to be greatly influenced by the airfoil deformation. The force and moment coefficients then begin to decrease as a result of the LEV lifting-off from the airfoil surface. Even though the LEV strength and size are actually increasing during this phase, its influence on the force and moment subsides as the low pressure region that it creates moves away from the airfoil surface. To illustrate this effect, the pressure field is provided in Fig. 16 for the rigid airfoil.

Furthermore, at approximately the mid-downstroke, the flexible TE airfoil is shown to produce the largest force, followed by the flexible LE and then the rigid airfoils. After reaching a local minima, both the force and moment coefficients begin to slightly increase. Siala and Liburdy[32] have previously shown that this increase in the forces is associated with the advection of the LEV along the airfoil chord. Shortly after the secondary peak, the force coefficient for the rigid and flexible TE drops rapidly, eventually switching sign at $t/T \approx 0.40$ (negative lift). On the other hand, the drop in lift force is shown to delay to $t/T \approx 0.42$ for the flexible TE airfoil. This is because the flexible TE airfoil suppresses the formation of TEV, thereby delaying its negative

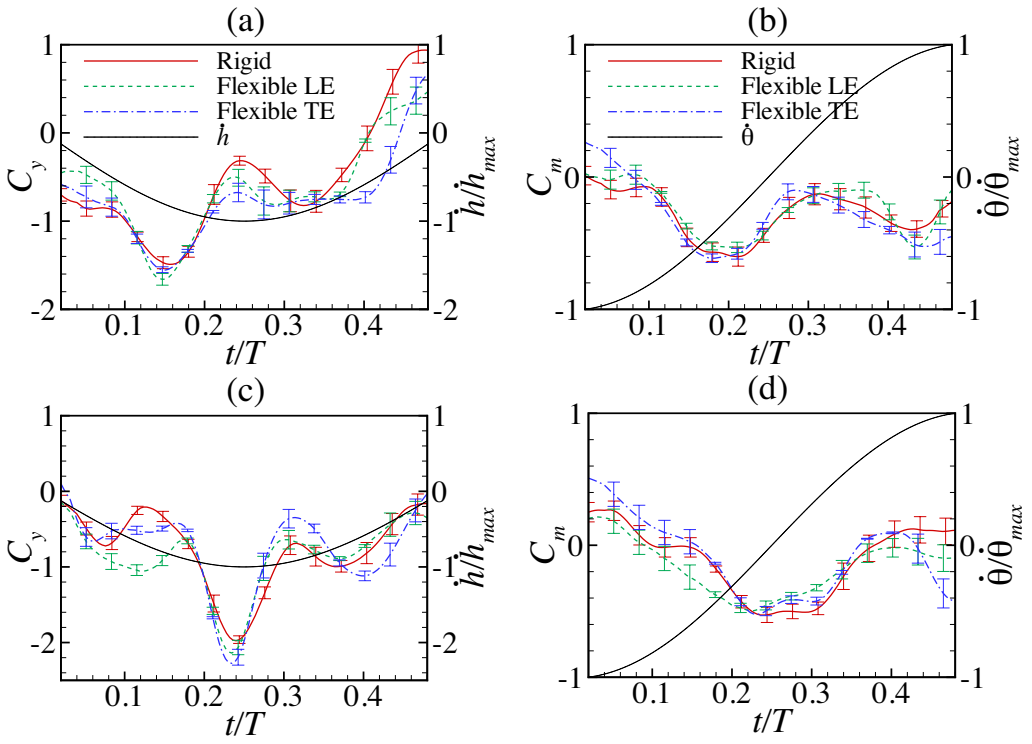

FIG. 15. Vertical force and pitching moment coefficients for (a,b) $k = 0.10$ and (c,d) $k = 0.14$. The dotted line represents the heaving and pitching velocities.

effects on the force coefficient. Moreover, the moment coefficients for the rigid and flexible LE airfoils approach $C_m \approx 0$ towards the end of the cycle, whereas for the flexible TE case, the moment coefficient remains relatively large and negative. Again, this is a result of the large TEV forming and rolling on the lower surface of the trailing edge for the rigid and flexible LE case. The pressure distribution for all three cases at $t/T = 0.45$ is shown in Fig. 17. For the rigid and flexible LE airfoils, the low pressure region created by the rolled TEV seems to be well balanced by the low pressure region on the upper surface of the airfoil, thus creating a relatively small pressure differential across the two surfaces. Conversely, the low pressure region on the top surface of the flexible TE airfoil is much lower than the pressure on the bottom surface. Since the low pressure region is concentrated in the downstream half of the airfoil, a negative counter-clockwise moment is generated.

As k is increased to 0.14, it can be seen that the peak force coefficient is delayed to slightly before mid-downstroke for all three cases. Similar to $k = 0.10$, the peak force is shown to be enhanced by the surface deformation, with the flexible TE airfoil generating a slightly larger peak

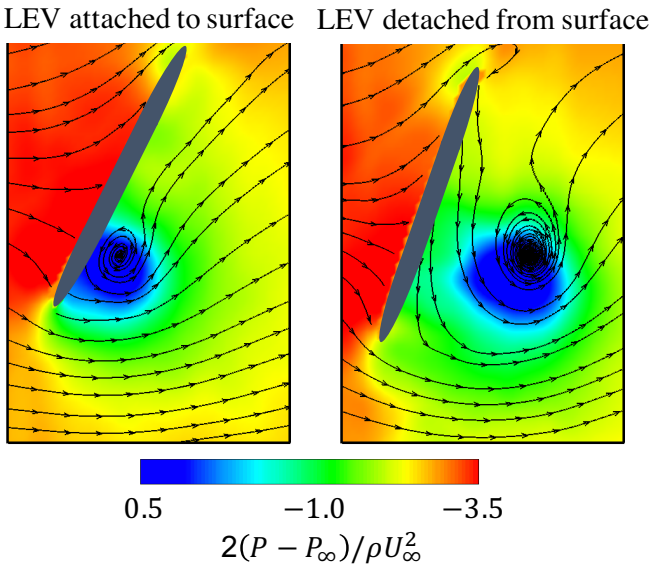

FIG. 16. Zoomed-in view of the pressure contour and streamlines at $k = 0.10$ showing an attached and detached LEV from the airfoil surface.

than the flexible LE airfoil. At this reduced frequency, the magnitude of peak force plays a much larger role in power generation than for $k = 0.10$, since its timing is well correlated with the timing of maximum heaving velocity. Furthermore, the effect of airfoil deformation remains minimal and less obvious on the peak moment coefficient. It can be anticipated that the magnitude of peak moment does not play an important role in power generation, since at this k value, it occurs when the pitching velocity is quite small. Toward the end of the downstroke, it can be seen that the flexible TE case generates a large negative moment relative to the rigid and flexible LE cases. This can be explained by examining the pressure distribution around the airfoil in Fig. 18. As a result of the secondary vortex that forms by the flexible TE airfoil near the leading edge, a low pressure zone is created that results in a negative counter-clockwise moment about the pitching axis. This low pressure region is not produced by the rigid and flexible LE airfoils.

F. Energy harvesting performance

In Fig. 19, we report the instantaneous power coefficient of the rigid, flexible LE and flexible TE airfoils for $k = 0.10$, 0.14 and 0.18. The power coefficient is defined as:

$$C_P = \frac{P}{1/2\rho U_\infty^3 c} \tag{14}$$

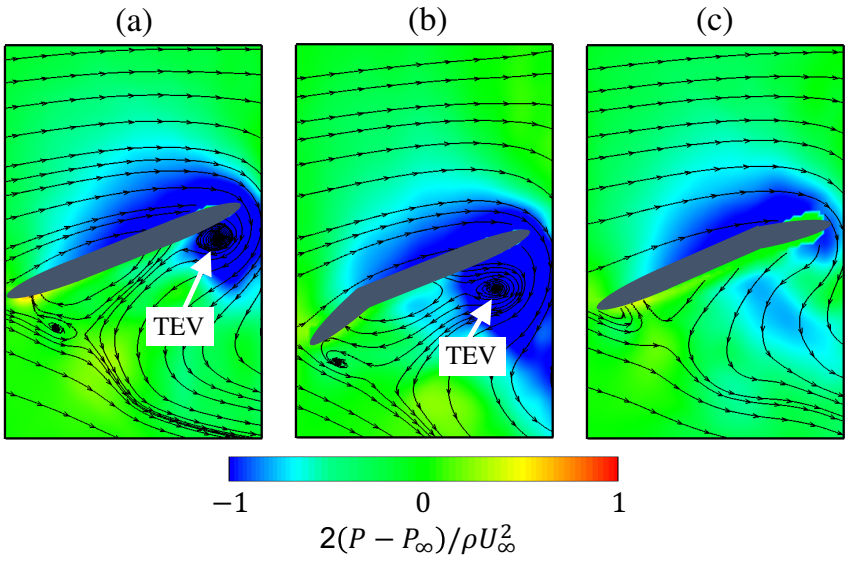

FIG. 17. Zoomed-in view of the pressure distribution and streamlines for $k = 0.10$ at $t/T = 0.45$ for (a) rigid, (b) flexible LE and (c) flexible TE airfoils.

where P is given in Eq. (1). At $k = 0.10$, the effect of leading/trailing edge deformation on power output is shown to be insignificant. For all cases, the power output has a positive sign throughout the majority of the downstroke, and becomes negative when $t/T > 0.4$. As k is increased to 0.14 and 0.18, the airfoil deformation begins to have a more pronounced effect. Early in the downstroke, the power output for all cases is shown to be negative, because the moment coefficient and pitching velocity have a negative correlation. Significantly enhanced peak powers are generated for all cases compared to $k = 0.10$, with the flexible TE and LE airfoils producing a slightly higher maximum power than the rigid airfoil.

The energy harvesting efficiency is defined as the ratio of mean power output to the available fluid power in the swept area of the airfoil:

$$\eta = \frac{\overline{P}}{1/2\rho U_\infty^3 d} \tag{15}$$

where $\overline{P}$ is the cycle-averaged power and d is the total crossflow distance swept by the airfoil. In addition, the energy harvesting efficiency can be decomposed into contributions of heaving and pitching motions as follows:

$$\eta_h = \frac{\overline{F_y \dot{h}}}{1/2\rho U_\infty^3 d} \tag{16}$$

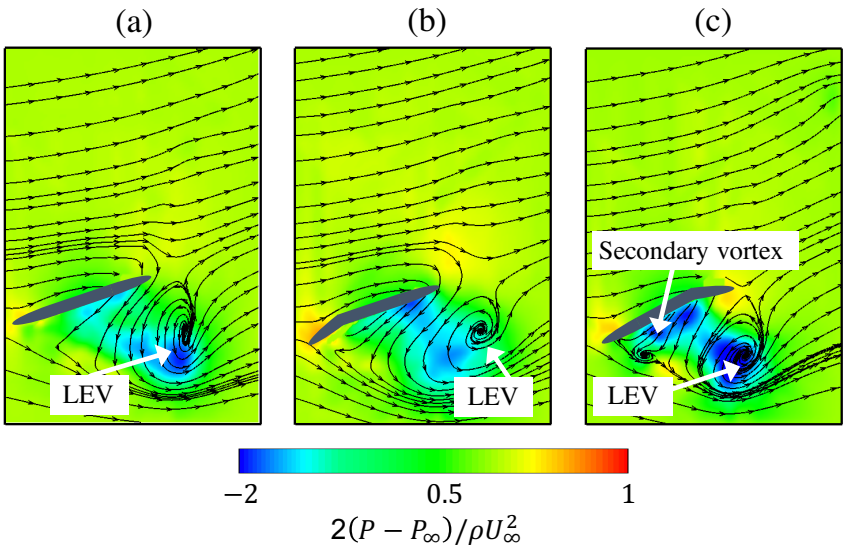

FIG. 18. Pressure distribution and streamlines for $k = 0.14$ at $t/T = 0.45$ for (a) rigid, (b) flexible LE and (c) flexible TE airfoils.

$$\eta_\theta = \frac{\overline{M_z \dot{\theta}}}{1/2\rho U_\infty^3 d} \tag{17}$$

The total energy harvesting efficiency, and the contributions of the heaving and pitching motions are shown in Fig. 20 as a function of reduced frequency. Note that two additional points are included for the rigid airfoil at $k = 0.12$ and $k = 0.16$ from a previous study[18]. At $k = 0.10$, it is shown in Fig. 20(a) that airfoil deformation at the leading and trailing edges slightly decrease the total energy harvesting efficiency compared to the rigid airfoil. The rigid airfoil produces power at an efficiency of 13.5%, whereas the flexible LE and TE operate at $\eta = 12.9\%$ and $\eta = 12.4\%$, respectively. While the contribution of heaving motion of the flexible TE airfoil is larger than the rigid and flexible TE airfoils, its pitching contribution is slightly more negative, as shown in Fig. 20(b) and 20(c), respectively. This is consistent with the results obtained by Totpal *et al.*[17], who have shown that at low reduced frequencies, surface deformation decreases the energy harvesting efficiency. As k is increased to 0.14, the total energy harvesting efficiency for the rigid and flexible LE airfoils increase up to $\eta = 25.1\%$ and 25.9%, whereas the efficiency of the flexible TE airfoil is increased to only $\eta = 16.5\%$. The slow rate of increase in η with increasing k of the flexible TE is a result of the large negative pitching efficiency that it produces, as shown in Fig. 20(c). This is a result of the secondary vortex that is formed by the flexible TE airfoil, which generates a

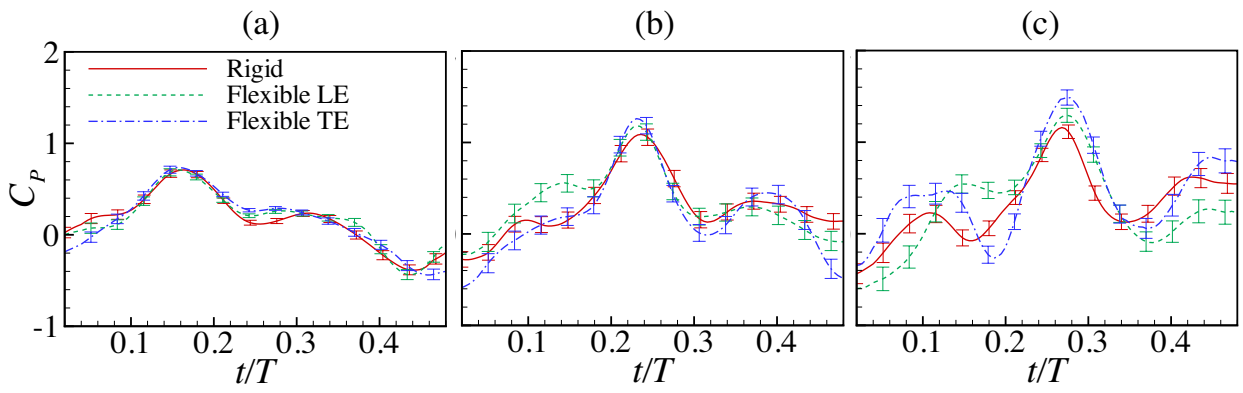

FIG. 19. Power coefficient of the rigid, flexible LE and flexible TE airfoils for (a) $k = 0.10$, (b) $k = 0.14$ and (c) $k = 0.18$.

relatively large negative moment while it has a large positive pitching velocity. When k is increased to 0.18, the total efficiency for the rigid airfoil begins to slowly decrease. Although the heaving contribution increases when k is increased, the negative pitching contribution is increased from $\eta_\theta = -2.6\%$ to $\eta_\theta = -6.5\%$. This trend of negative increase in pitching contributions at high reduced frequencies has been reported by multiple authors in the literature[16,30]. Furthermore, the flexible LE airfoil is shown to have a greater heaving contribution when compared to the rigid, while its pitching contribution is more negative than the rigid airfoil. On the other hand, the negative contribution of the pitching motion of flexible TE airfoil is shown to drop from $\eta_\theta = -8.1\%$ to $\eta_\theta = -4.9\%$ at $k = 0.14$ and $k = 0.18$, respectively, which results in a greater overall efficiency at $k = 0.18$ compared to the flexible LE airfoil. The shift to higher reduced frequency for peak efficiency for both flexible LE and TE compared to the rigid airfoil has also been observed by Liu *et al.*[28]

IV. CONCLUSIONS

The effects of inertia-induced deformation of the leading and trailing edges of the airfoil on the flow physics and power extraction performance of an oscillating energy harvester were experimentally studied using wind tunnel testing. Two-dimensional particle image velocimetry measurements were conducted at reduced frequencies of $k = 0.10$, 0.14 and 0.18, with pitching and heaving amplitudes fixed at $\theta_0 = 75^\circ$ and $h_0 = 0.6c$, respectively. The velocity data from the particle image velocimetry measurements were used to analyze the dynamics of the leading edge vortex, as well

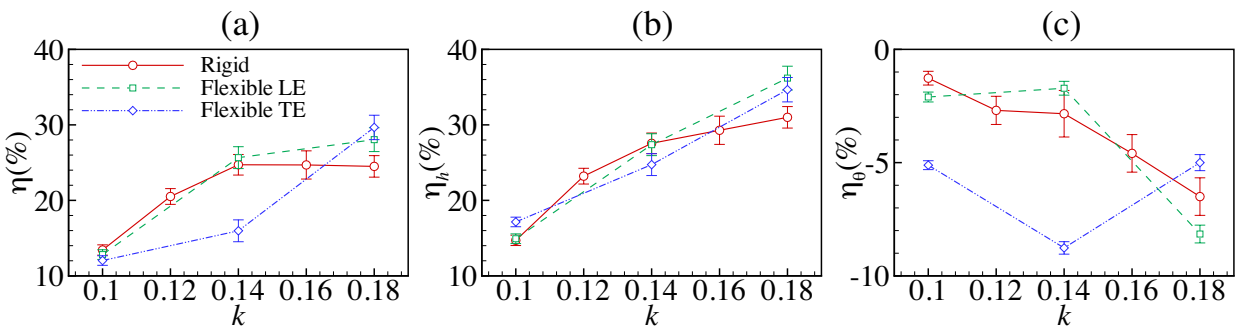

FIG. 20. (a) Total energy harvesting efficiency, (b)heaving contribution and (c) pitching contribution versus reduced frequency.

as to calculate force and pitching moment using the vortex-impulse theory.

The results show that the evolution of the leading edge vortex is altered by using a deforming airfoil surface. The timing of the leading edge vortex inception was shown to be slightly shifted to earlier times during the oscillation cycle, thereby slightly shifting the force peaks to earlier times relative to the rigid airfoil. The deforming leading edge directly influences the initiation of the leading edge vortex by altering the flow conditions at the airfoil leading edge tip. On the other hand, the deforming trailing edge is believed to increase the effective camber of the airfoil, which also alters the flow at the leading edge. It is argued that for both cases, the vorticity flux from the leading edge is increased as a result of the enhanced flow at the leading edge of the airfoil. In addition, it was shown that the inception time of the leading edge vortex for both the rigid and flexible leading edge airfoils coincides with the time at which the non-dimensional shear layer velocity reaches a value of approximately 0.5. Furthermore, the time-history of the leading edge vortex was analyzed. The results show that deformation at the leading edge of the airfoil enhances the growth rate and maximum strength of the LEV at $k = 0.10$ and $k = 0.14$ compared to the rigid and flexible trailing edge airfoils, while for $k = 0.18$, the LEV circulation for all three cases is essentially identical. For both the flexible leading edge and rigid airfoils, the trailing edge shear layer was observed to roll-up into a large trailing edge vortex at $k = 0.10$, which is responsible for cutting-off the vorticity supply from the shear layer to the leading edge vortex, in a mechanism known in the literature as bluff-body vortex detachment. Conversely, the motion of the flexible trailing edge suppresses the formation of the trailing edge vortex, and the leading edge vortex is believed to be detached from its shear layer via the boundary layer eruption mechanism. When

$k > 0.10$, none of the airfoils generate a trailing edge vortex, and the boundary layer eruption mechanism is proposed to be responsible for cutting off the vorticity supply to the leading edge vortex.

The instantaneous power output and energy harvesting efficiency of the deforming leading and trailing edge airfoils were compared with the rigid airfoil. At $k = 0.10$, no performance enhancement was observed by the flexible leading and trailing edge airfoils compared to the rigid airfoil. However, they are shown to be more effective at $k = 0.18$, where the energy harvesting efficiency was shown to increase to 30% and 28%, respectively, compared to the 24% efficiency of the rigid airfoil. The rigid airfoil efficiency is shown to peak at $k = 0.14$, whereas both deforming airfoils peak at $k = 0.18$, agreeing quite well with results reported in the literature.

The results of this study experimentally validate the feasibility of using deforming airfoil surface to enhance the performance of oscillating energy harvesters. Future work will be conducted at larger reduced frequencies to determine the optimal operating reduced frequency of the flexible leading and trailing edge airfoils.

ACKNOWLEDGEMENT

The authors would like to acknowledge the financial support provided by the Air Force Office of Scientific Research Under the MURI grant FA9550-07-1-0540 and the National Science Foundation CBET Award Number 1804964. Firas Siala also acknowledges the financial support from Link Energy Foundation Fellowship.

REFERENCES

[1]R. Saidur, N. Rahim, M. Islam, and K. Solangi, "Environmental impact of wind energy," Renewable and Sustainable Energy Reviews **15**, 2423–2430 (2011).

[2]T. Kinsey and G. Dumas, "Parametric study of an oscillating airfoil in a power-extraction regime," AIAA Journal **46**, 1318–1330 (2008).

[3]Q. Zhu, "Optimal frequency for flow energy harvesting of a flapping foil," Journal of Fluid Mechanics **675**, 495–517 (2011).

[4]T. Kinsey and G. Dumas, "Computational fluid dynamics analysis of a hydrokinetic turbine based on oscillating hydrofoils," Journal of Fluids Engineering **134**, 021104 (2012).

[5]P. Ma, Z. Yang, Y. Wang, H. Liu, and Y. Xie, "Energy extraction and hydrodynamic behavior analysis by an oscillating hydrofoil device," Renewable Energy **113**, 648–659 (2017).

[6]J. Young, J. C. Lai, and M. F. Platzer, "A review of progress and challenges in flapping foil power generation," Progress in Aerospace Sciences **67**, 2–28 (2014).

[7]S. P. Sane, "The aerodynamics of insect flight," Journal of Experimental Biology **206**, 4191–4208 (2003).

[8]S. Ho, H. Nassef, N. Pornsinsirirak, Y.-C. Tai, and C.-M. Ho, "Unsteady aerodynamics and flow control for flapping wing flyers," Progress in Aerospace Sciences **39**, 635–681 (2003).

[9]W. Shyy, Y. Lian, J. Tang, D. Viieru, and H. Liu, *Aerodynamics of low Reynolds number flyers*, Vol. 22 (Cambridge University Press, 2007).

[10]D. D. Chin and D. Lentink, "Flapping wing aerodynamics: from insects to vertebrates," Journal of Experimental Biology **219**, 920–932 (2016).

[11]E. C. Polhamus, "Predictions of vortex-lift characteristics by a leading-edge suctionanalogy," Journal of Aircraft **8**, 193–199 (1971).

[12]I. H. Tuncer and M. F. Platzer, "Computational study of flapping airfoil aerodynamics," Journal of Aircraft **37**, 514–520 (2000).

[13]I. H. Tuncer and M. Kaya, "Optimization of flapping airfoils for maximum thrust and propulsive efficiency," AIAA Journal **43**, 2329–2336 (2005).

[14]G. Dumas and T. Kinsey, "Eulerian simulations of oscillating airfoils in power extraction regime," WIT Transactions on Engineering Sciences **52** (2006).

[15]M. Ashraf, J. Young, and J. Lai, "Reynolds number, thickness and camber effects on flapping airfoil propulsion," Journal of Fluids and Structures **27**, 145–160 (2011).

[16]D. Kim, B. Strom, S. Mandre, and K. Breuer, "Energy harvesting performance and flow structure of an oscillating hydrofoil with finite span," Journal of Fluids and Structures **70**, 314–326 (2017).

[17]A. D. Totpal, F. F. Siala, and J. A. Liburdy, "Energy harvesting of an oscillating foil at low reduced frequencies with rigid and passively deforming leading edge," Journal of Fluids and Structures **82**, 329–342 (2018).

[18]F. F. Siala and J. A. Liburdy, "Power estimation of flapping foil energy harvesters using vortex impulse theory," Renewable Energy, Under Review (2019).

[19]M. Ashraf, J. Young, J. S. Lai, and M. Platzer, "Numerical analysis of an oscillating-wing wind and hydropower generator," AIAA Journal **49**, 1374–1386 (2011).

[20]T. Q. Le, J. H. Ko, and D. Byun, "Morphological effect of a scallop shell on a flapping-type tidal stream generator," Bioinspiration & Biomimetics **8**, 036009 (2013).

[21]Y. Xie, K. Lu, and D. Zhang, "Investigation on energy extraction performance of an oscillating foil with modified flapping motion," Renewable Energy **63**, 550–557 (2014).

[22]K. Lu, Y. Xie, D. Zhang, and G. Xie, "Systematic investigation of the flow evolution and energy extraction performance of a flapping-airfoil power generator," Energy **89**, 138–147 (2015).

[23]J.-M. Miao and M.-H. Ho, "Effect of flexure on aerodynamic propulsive efficiency of flapping flexible airfoil," Journal of Fluids and Structures **22**, 401–419 (2006).

[24]L. Zhao, X. Deng, and S. P. Sane, "Modulation of leading edge vorticity and aerodynamic forces in flexible flapping wings," Bioinspiration & Biomimetics **6**, 036007 (2011).

[25]T. Nakata, H. Liu, Y. Tanaka, N. Nishihashi, X. Wang, and A. Sato, "Aerodynamics of a bio-inspired flexible flapping-wing micro air vehicle," Bioinspiration & Biomimetics **6**, 045002 (2011).

[26]D. Cleaver, I. Gursul, D. Calderon, and Z. Wang, "Thrust enhancement due to flexible trailing-edge of plunging foils," Journal of Fluids and Structures **51**, 401–412 (2014).

[27]C. Hoke, J. Young, and J. Lai, "Effects of time-varying camber deformation on flapping foil propulsion and power extraction," Journal of Fluids and Structures **56**, 152–176 (2015).

[28]W. Liu, Q. Xiao, and F. Cheng, "A bio-inspired study on tidal energy extraction with flexible flapping wings," Bioinspiration & Biomimetics **8**, 036011 (2013).

[29]F.-B. Tian, J. Young, and J. C. Lai, "Improving power-extraction efficiency of a flapping plate: From passive deformation to active control," Journal of Fluids and Structures **51**, 384–392 (2014).

[30]Z. Liu, F.-B. Tian, J. Young, and J. C. Lai, "Flapping foil power generator performance enhanced with a spring-connected tail," Physics of Fluids **29**, 123601 (2017).

[31]J.-Z. Wu, H.-Y. Ma, and M.-D. Zhou, *Vorticity and vortex dynamics* (Springer Science & Business Media, 2007).

[32]F. F. Siala and J. A. Liburdy, "Leading edge vortex dynamics and impulse-based lift force analysis of oscillating airfoils," Experiments in Fluids, Under Review (2019).

[33]A. D. Totpal, *The energy extraction performance of an oscillating rigid and flexible foil*, Master's thesis (2017).

[34]Q. Xiao and Q. Zhu, "A review on flow energy harvesters based on flapping foils," Journal of Fluids and Structures **46**, 174–191 (2014).

[35]B. Wieneke, "Piv uncertainty quantification from correlation statistics," Measurement Science and Technology **26**, 074002 (2015).

[36]F. Siala, *Experimental investigations of the unsteady aerodynamics of oscillating airfoil energy harvesters*, Ph.D. thesis, Oregon State University (2019).

[37]J. C. Wu, "Theory for aerodynamic force and moment in viscous flows," AIAA Journal **19**, 432–441 (1981).

[38]J. Lighthill, "An informal introduction to theoretical fluid mechanics," (1986).

[39]P. G. Saffman, *Vortex dynamics* (Cambridge university press, 1992).

[40]F. Noca, *On the evaluation of time-dependent fluid-dynamic forces on bluff bodies*, Ph.D. thesis, California Institute of Technology (1997).

[41]A. C. DeVoria, Z. R. Carr, and M. J. Ringuette, "On calculating forces from the flow field with application to experimental volume data," Journal of Fluid Mechanics **749**, 297–319 (2014).

[42]J. O. Dabiri, S. Bose, B. J. Gemmell, S. P. Colin, and J. H. Costello, "An algorithm to estimate unsteady and quasi-steady pressure fields from velocity field measurements," Journal of Experimental Biology **217**, 331–336 (2014).

[43]D. E. Rival, J. Kriegseis, P. Schaub, A. Widmann, and C. Tropea, "Characteristic length scales for vortex detachment on plunging profiles with varying leading-edge geometry," Experiments in Fluids **55**, 1660 (2014).

[44]A. Widmann and C. Tropea, "Parameters influencing vortex growth and detachment on unsteady aerodynamic profiles," Journal of Fluid Mechanics **773**, 432–459 (2015).

[45]F. F. Siala, A. D. Totpal, and J. A. Liburdy, "Optimal leading edge vortex formation of a flapping foil in energy harvesting regime," in *ASME 2017 Fluids Engineering Division Summer Meeting* (American Society of Mechanical Engineers, 2017) pp. V01CT23A008–V01CT23A008.

[46]C. H. Williamson and A. Roshko, "Vortex formation in the wake of an oscillating cylinder," Journal of Fluids and Structures **2**, 355–381 (1988).

[47]J. G. Wong and D. E. Rival, "Determining the relative stability of leading-edge vortices on nominally two-dimensional flapping profiles," Journal of Fluid Mechanics **766**, 611–625 (2015).

[48]J. D. Eldredge and A. R. Jones, "Leading-edge vortices: mechanics and modeling," Annual Review of Fluid Mechanics **51**, 75–104 (2019).

[49]K. Ramesh, A. Gopalarathnam, K. Granlund, M. V. Ol, and J. R. Edwards, "Discrete-vortex method with novel shedding criterion for unsteady aerofoil flows with intermittent leading-edge vortex shedding," Journal of Fluid Mechanics **751**, 500–538 (2014).

[50]L. Graftieaux, M. Michard, and N. Grosjean, "Combining piv, pod and vortex identification algorithms for the study of unsteady turbulent swirling flows," Measurement Science and Technology **12**, 1422 (2001).

[51]T. Doligalski, C. Smith, and J. Walker, "Vortex interactions with walls," Annual Review of Fluid Mechanics **26**, 573–616 (1994).